JGR Atmospheres

RESEARCH ARTICLE
10.1029/2020JD032513

Special Section:
Southern Ocean Clouds, Aerosols, Precipitation and Radiation

Structure of an Atmospheric River Over Australia and the Southern Ocean. Part I: Tropical and Midlatitude Water Vapor Fluxes

Robert M. Rauber[1], Huancui Hu[2], Francina Dominguez[1], Stephen W. Nesbitt[1], Greg M. McFarquhar[3], Troy J. Zaremba[1], and Joseph A. Finlon[1,4]

[1]Department of Atmospheric Sciences, University of Illinois at Urbana–Champaign, Urbana and Champaign, IL, USA, [2]Atmospheric Sciences and Global Change Division, Pacific Northwest National Laboratory, Richland, WA, USA, [3]Cooperative Institute for Mesoscale Meteorological Studies and School of Meteorology, University of Oklahoma, Norman, OK, USA, [4]Now at Department of Atmospheric Sciences, University of Washington, Seattle, WA, USA

This article is a companion to Finlon et al. (2020), https://doi.org/10.1029/2020JD032514.

Key Points:
- The contribution of moisture from the tropics to precipitation within an Australian summer atmospheric river is documented
- Over 50% of the moisture arriving at the Southern Ocean at altitudes above the 0°C isotherm was sourced from tropical latitudes
- The tropical contribution to precipitation decreased with latitude, >70% over Australia, ~50% off Australia, and <10% poleward of 60°S

Supporting Information:
- Supporting Information S1
- Movie S1

Correspondence to:
R. M. Rauber,
r-rauber@illinois.edu

Citation:
Rauber, R. M., Hu, H., Dominguez, F., Nesbitt, S. W., McFarquhar, G. M., Zaremba, T. J., et al. (2020). Structure of an atmospheric river over Australia and the Southern Ocean. Part I: Tropical and midlatitude water vapor fluxes. *Journal of Geophysical Research: Atmospheres*, *125*, e2020JD032513. https://doi.org/10.1029/2020JD032513

Received 3 FEB 2020
Accepted 7 SEP 2020
Accepted article online 11 SEP 2020

Author Contributions:
Conceptualization: Robert M. Rauber, Huancui Hu, Francina Dominguez, Greg M. McFarquhar
Formal analysis: Robert M. Rauber, Huancui Hu, Francina Dominguez, Troy J. Zaremba, Joseph A. Finlon
(continued)

Abstract An atmospheric river (AR) impacting Tasmania, Australia, and the Southern Ocean during the austral summer on 28–29 January 2018 during the Southern Ocean Clouds, Radiation, Aerosol Transport Experimental Study campaign is analyzed using a modeling and observational approach. Gulfstream-V dropsonde measurements and Global Precipitation Measurement radar analyses were used in conjunction with Weather Research and Forecasting model simulations with water vapor tracers to investigate the relative contributions of tropical and midlatitude moisture sources to the AR. Moisture associated with a monsoonal tropical depression became entrained into a midlatitude frontal system that extended to 60°S, reaching the associated low-pressure system 850 km off the coast of Antarctica—effectively connecting the tropics and the polar region. Tropical moisture contributed to about 50% of the precipitable water within the AR as the flow moved over the Southern Ocean near Tasmania. The tropical contribution to precipitation decreased with latitude, from >70% over Australia, to ~50% off the Australian coast, to less than 5% poleward of 55°S. The integrated vapor transport (IVT) through the core of the AR reached above 500 kg m^{-1} s^{-1} during 1200 UTC 28 January to 0600 UTC 29 January, 1.29 times the average amount of water carried by the world's largest terrestrial river, the Amazon. The high IVT strength might be attributed to the higher water vapor content associated with the warmer temperatures across Australia and the Southern Ocean in austral summer.

Plain Language Summary Atmospheric rivers (ARs) are long, narrow corridors of strong horizontal water vapor transport, normally associated with a low-level jet stream ahead of a cold front. They play a critical role in the global hydrologic cycle and have been studied extensively over the northeast Pacific. This and a companion paper are the first to analyze an AR event impacting Tasmania, Australia, and the Southern Ocean using a modeling and observational approach. The AR extended from the tropics over northern Australia southeastward to the southern Australian coast and over the Southern Ocean to 60°S. The flow at higher altitudes in the AR was primarily composed of moisture originating in the tropics, while at lower altitudes and warmer temperatures, the moisture was primarily sourced from middle latitudes as a result of the circulation associated with a cold front. The tropical contribution to precipitation decreased with latitude, from >70% over Australia, to ~50% off the Australian coast, to less than 5% poleward of 55°S. Water vapor transported through the core of the AR was more than the average amount of water carried by the world's largest river, the Amazon, during the same time interval.

1. Introduction

Atmospheric rivers (ARs) play a critical role in the global hydrologic cycle as 90% of the meridional moisture flux in the extratropics occurs along these filamentary structures associated with the low-level jet stream ahead of the cold front of extratropical cyclones (American Meteorological Society, 2020; Ralph et al., 2018; Zhu & Newell, 1998). When ARs make landfall, they are often associated with strong winds, precipitation, and flooding (Gimeno et al., 2016; Waliser & Guan, 2017). Many studies of ARs focus on the U.S. West Coast as major flooding events in river valleys emerging from mountain ranges along the West Coast often are associated with landfalling ARs (Dettinger et al., 2011; Hu et al., 2017; Leung & Qian, 2009; Neiman,

Funding acquisition: Robert M. Rauber, Greg M. McFarquhar
Investigation: Robert M. Rauber, Francina Dominguez, Joseph A. Finlon
Methodology: Robert M. Rauber, Huancui Hu, Francina Dominguez, Stephen W. Nesbitt, Greg M. McFarquhar, Troy J. Zaremba, Joseph A. Finlon
Project administration: Greg M. McFarquhar
Software: Troy J. Zaremba, Joseph A. Finlon
Writing - original draft: Robert M. Rauber, Francina Dominguez
Writing – review & editing: Robert M. Rauber, Huancui Hu, Francina Dominguez, Greg M. McFarquhar, Joseph A. Finlon

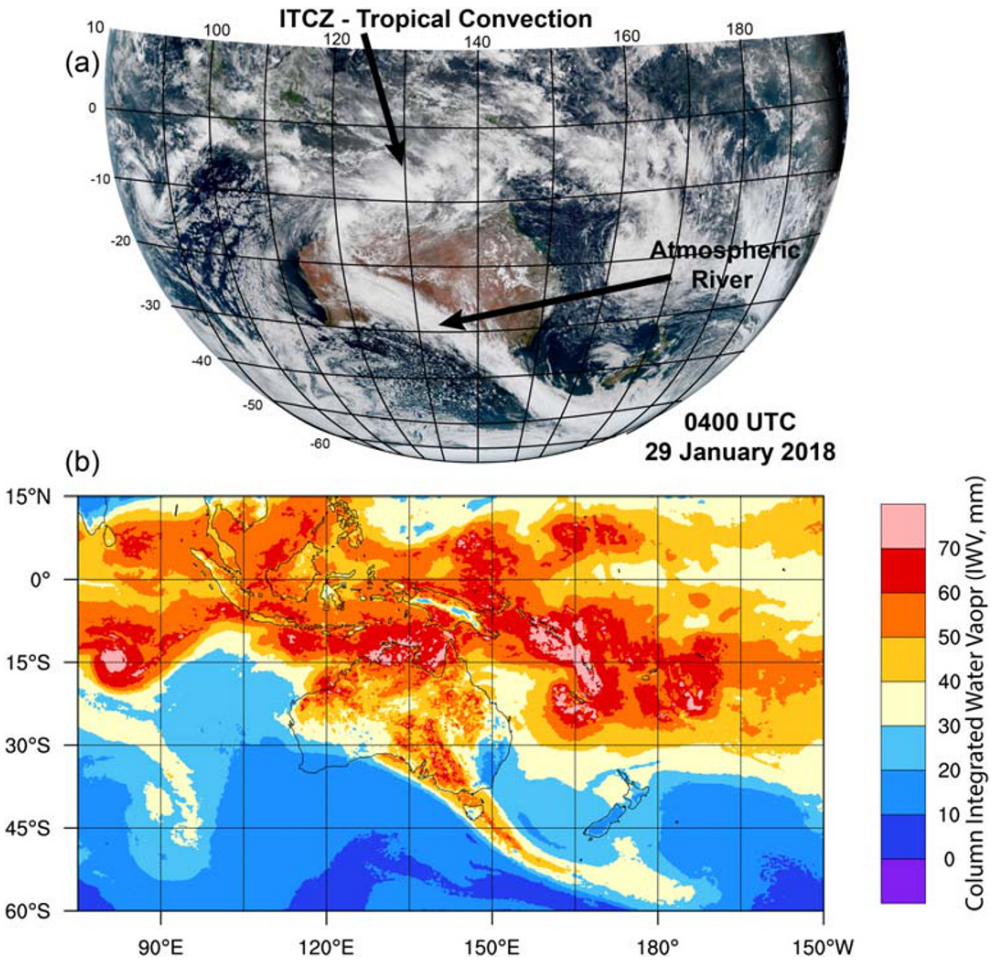

Figure 1. (a) Visible satellite image of the Southern Hemisphere from the Himawari 8 satellite showing the cloud field associated with the atmospheric river and tropical convection along the Intertropical Convergence Zone (ITCZ) at 0400 UTC 29 January 2018. (b) Satellite imagery of total column water vapor (IWV) at the same time as the visible satellite image (data from http://tropic.ssec.wisc.edu/real-time/mtpw2/).

Ralph, Wick, Kuo, et al., 2008; Neiman, Ralph, Wick, Lundquist, & Dettinger, 2008; Ralph et al., 2004, 2006 among many others). Extreme hydrometeorological impacts related to ARs have also been well documented in regions such as the west coast of Europe (Lavers & Villarini, 2013; Lavers et al., 2011; Ramos et al., 2015; Stohl et al., 2008). ARs in the Southern Hemisphere have not received as much attention, with the exception of events affecting South America (Viale & Nunez, 2011; Viale et al., 2018).

To date, however, little information is available concerning ARs impacting Australia, the Southern Ocean, and the Antarctic coast. Western Australia is an important source region for the poleward transport of tropical moisture (Knippertz et al., 2013). Global analyses of ARs show that ARs affect the coast of southern Australia on average about every 10 days. Half of those ARs produce locally heavy precipitation, particularly on the southwest coast near Tasmania (Waliser & Guan, 2017). Paltan et al. (2017) found that ARs over Australia contribute little if anything to runoff, total soil moisture content, or snow water equivalent. However, this same study finds that when they do occur, ARs are associated with extreme flows, particularly in southeast Australia. Waliser and Guan (2017) show that ARs are common over the Southern Ocean, a region of frequent AR termination (Guan & Waliser, 2019). When AR structures penetrate poleward toward Antarctica, they are associated with extreme tropospheric water vapor anomalies (Gorodetskaya et al., 2020). More than half of the precipitation variance south of 70°S can be explained by AR-related vapor transport (Nash et al., 2018). In fact, Gorodetskaya et al. (2014) show that ARs impact precipitation over the Antarctic coastline, and in some years, nearly 80% of the outstanding ice sheet surface mass balance can

Table 1
Dropsonde Sensor Specifications

	Range	Repeatability	Resolution
Pressure	100–1,080 hPa	±0.5 hPa	0.1 hPa
Temperature	−90 to +60°C	±0.2°C	0.1°C
Relative humidity	0–100%	±5%	1.0%
Wind speed and direction	0–200 m s^{-1}, 0–360°	±0.5 m s^{-1}, ±2°	0.1 m s^{-1}, 1°

be attributed to a few AR-related events. Antarctic ARs can also be accompanied by warm temperature anomalies. Bozkurt et al. (2018) and Wille et al. (2019) found that Antarctic ARs can be associated with a large percentage of major surface melt occurrences.

ARs can be identified through analysis of total column integrated water vapor (IWV) or integrated vapor transport (IVT) using observations, models, and/or reanalysis data (see Shields et al., 2018 for a comprehensive review). Using back trajectory analysis, Ryoo et al. (2015) showed that U.S. West Coast ARs can originate in the extratropics or tropics/subtropics. In the Southern Hemisphere, the region of Western Australia and adjacent oceans is characterized by significant poleward transport of tropical moisture, such that nearly 60% of total meridional moisture transport in the Southern Hemisphere summer is of direct tropical origin (Knippertz et al., 2013). It is important to keep in mind, however, that numerically evaluating the geographical origin of atmospheric moisture requires the use of water vapor tracing models (see a review of methods in Gimeno et al., 2012 and Dominguez et al., 2020). Some extreme AR precipitation events have been associated with very high moisture content of tropical origin (Eiras Barca et al., 2017). However, there is also strong evidence that in many cases, tropical moisture rains out along the AR, while the characteristic signature of high moisture transport along the AR is sustained by local evaporation and continuous moisture

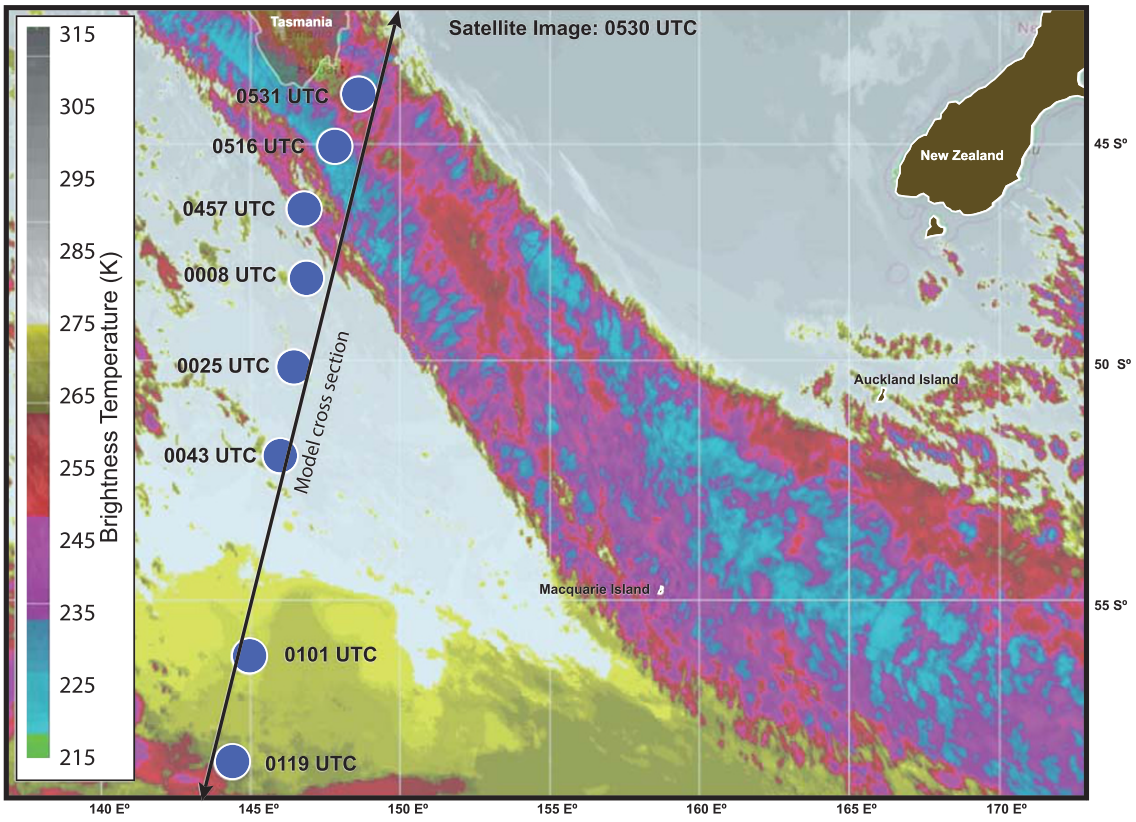

Figure 2. Himawari 8 enhanced thermal infrared image of the atmospheric river over the Southern Ocean on 29 January 2018 at 0530 UTC. The circles show dropsonde launch locations and times. The location of the model cross section (see Figure 8) is also shown.

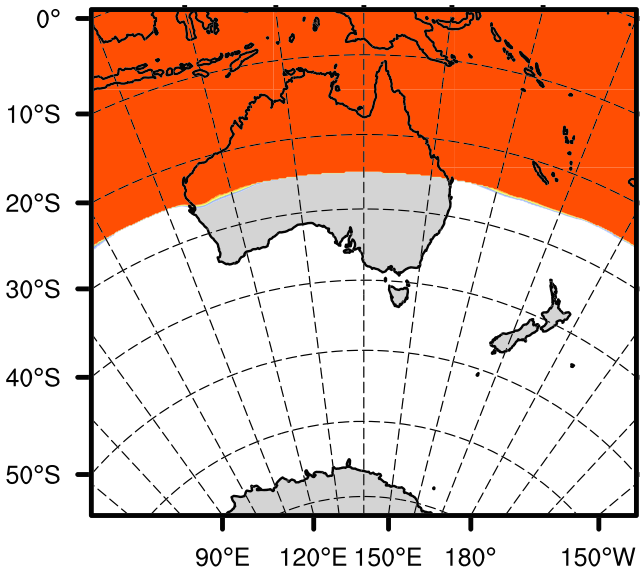

Figure 3. Model domain for the WRF simulation. Moisture originating within the orange area was tagged as tropical by the water vapor tracer module.

convergence ahead of the cold fronts associated with the extratropical cyclones (Bao et al., 2006; Dacre et al., 2015; Hu & Dominguez, 2019).

The situation is further complicated when ARs are dynamically associated with tropical cyclones (TCs). In these cases, large amounts of moisture near the TC that penetrate deep into the troposphere in the tropics can become entrained into midlatitude frontal systems (Cordeira et al., 2013). Careful moisture budget analysis reveals that either the tropical moisture rains out along the AR trajectory while IWV is maintained by convergence along the front (Cordeira et al., 2013) or that tropical moisture exports significantly contribute to precipitation as the AR makes landfall (Stohl et al., 2008).

An unanticipated opportunity to obtain detailed information on the structure and microphysics of an AR over Tasmania and the Southern Ocean occurred on 28 January 2018 (29 January in UTC) during the Southern Ocean Clouds, Radiation, Aerosol Transport Experimental Study (SOCRATES). The AR originated just off the northwest Australia coast at 10°S in the vicinity of the monsoon trough associated with the Intertropical Convergence Zone (ITCZ), with moisture flowing southeast across Australia, over Tasmania, and southeastward to a latitude of 60°S, south of New Zealand (Figure 1a). The cloud band associated with the AR was over 5,000 km long and ~500 km wide. Total column water vapor within the AR ranged from 30 to 70 mm (Figure 1b). In contrast to North American Pacific ARs that traverse large oceanic areas before making landfall, the plume of moisture in this Australian AR originated over the deep tropics at the ITCZ and passed nearly 3,500 km over the deserts of Western and Central Australia before moving off the coast of Tasmania and terminating over the Southern Ocean. During the event, the National Science Foundation (NSF)/National Center for Atmospheric Research (NCAR) Gulfstream-V (G-V) research aircraft ascended through the AR and later launched dropsondes across the AR.

This is the first of two papers filling critical gaps in our understanding of Southern Hemisphere ARs, particularly those affecting Australia and Tasmania. In Part I, the large-scale characteristics of the 28 January 2018 AR are presented using satellite, surface, and dropsonde measurements. A Weather Research and Forecasting (WRF) model simulation of the AR is then used to estimate (1) the relative contribution of the tropical monsoon trough moisture source versus midlatitude moisture sources to the flux of water vapor moving off the southeast Australia coast within the AR, (2) the vertical distribution of the moisture from these sources passing through the AR, and (3) the contribution to precipitation over the Southern Ocean from each moisture source within the AR. Unlike previous modeling approaches, this work uses WRF with embedded water vapor tracers that allow the moisture that originates from the tropics to be isolated and tracked. In Finlon et al. (2020) (hereafter, Part II), the detailed microphysical processes within the AR are examined using airborne radar and microphysical analyses from the research aircraft as it passed across and descended through the AR. The combination of aircraft observations and regional modeling is a powerful tool to analyze the dynamic and thermodynamic structure and precipitation processes within specific AR events (e.g., Cannon et al., 2020; Ryoo et al., 2020).

2. Data Sources

2.1. Dropsondes

The G-V aircraft was based in Hobart, Australia (42.88°S, 147.50°E), during SOCRATES. SOCRATES missions focused on Southern Ocean boundary layer clouds. SOCRATES standard flight procedures specified an ascent from the airport to 5,500 m, a level flight at 5,500 m to a latitude near 62°S, and then a return to Hobart. Dropsondes were launched on the southbound legs during SOCRATES flights while over the boundary layer clouds. The dropsondes were NCAR AVAPS™ Airborne Vertical Atmospheric Profiling Systems (Hock & Franklin, 1999; UCAR, 2020) incorporating a pressure, temperature, humidity sensor module (RSS903) designed by Vaisala, Inc., for their RS92 radiosonde and a GPS receiver module. A typical

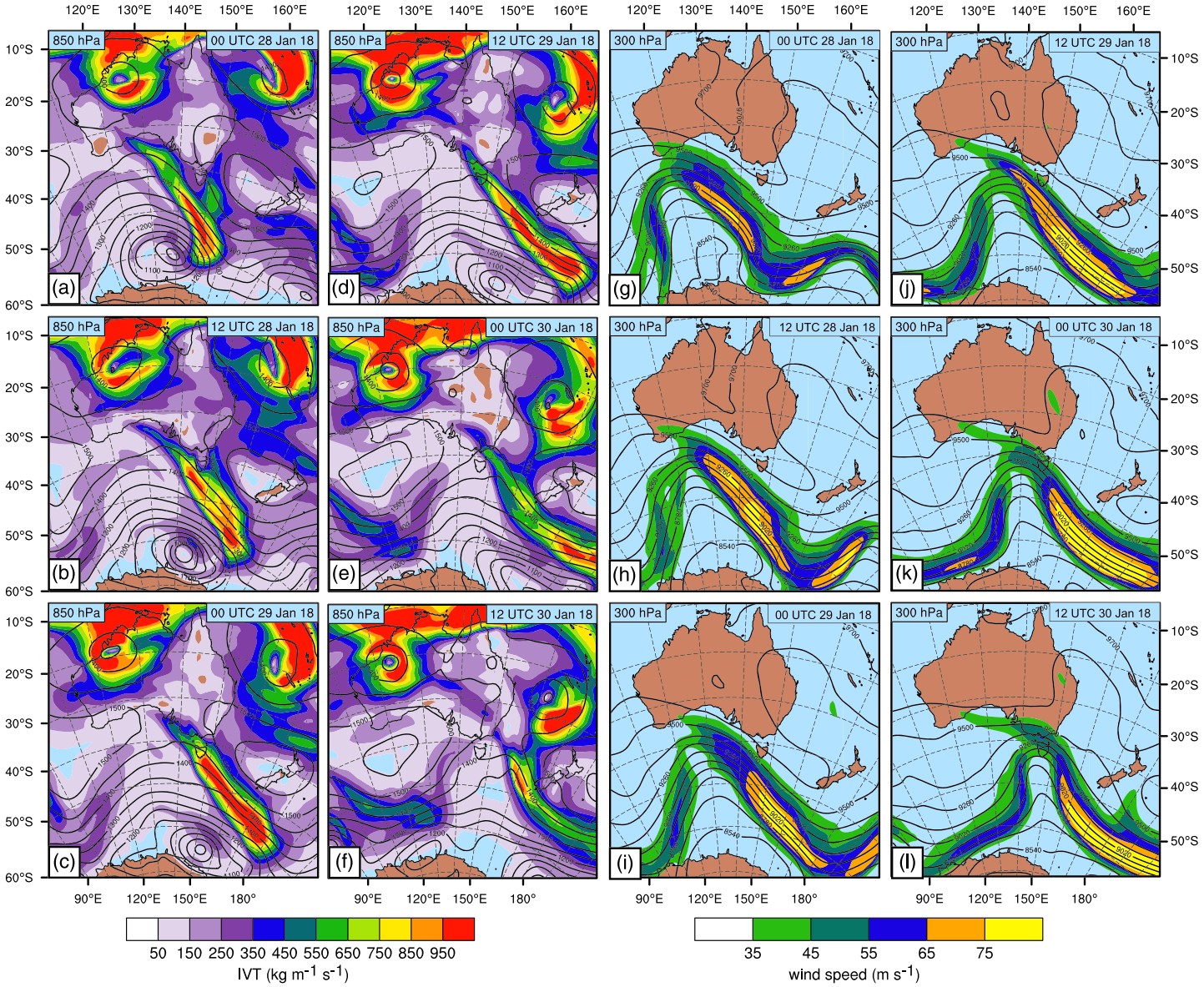

Figure 4. (a–f) Time series of 850 hPa analyses of geopotential height (solid lines, m) and integrated water vapor transport (kg m^{-1} s^{-1}) every 12 hr from 0000 28 January through 1200 UTC 30 January 2018; (g–l) time series of 300 hPa analyses of geopotential height (solid lines, m) and wind speed (colors, m s^{-1}) from 0000 UTC 28 January through 1200 UTC 30 January 2018 (analyses from ERA-Interim).

descent from 5.5 km took approximately 500 s during which thermodynamic and wind data were recorded at 0.5-s intervals. The average horizontal displacement between flight level and the surface was 8.4 km. The average vertical resolution of all dropsondes was 13.2 m. The dropsonde data were quality controlled to account for fast fall speeds during the first few minutes of descent, and a pressure correction was applied to the entire profile of each sounding during the quality control process with the median pressure correction of 1 hPa. The accuracy of the dropsonde sensors is ±0.2°C for temperature, ±0.5 m s^{-1} for wind speed, ±2° for wind direction, and ±5% for relative humidity. Dropsonde data were interpolated back to the closest great circle distance between the dropsonde position and the flight track and then linearly interpolated to a 2-D Cartesian grid to create a cross section. The sensor specifications are summarized in Table 1.

At the time of takeoff at 2250 UTC, 28 January 2018, the AR was located directly over Hobart. The aircraft ascended through the AR from the airport, exiting its southern boundary at 2340 UTC at an altitude of

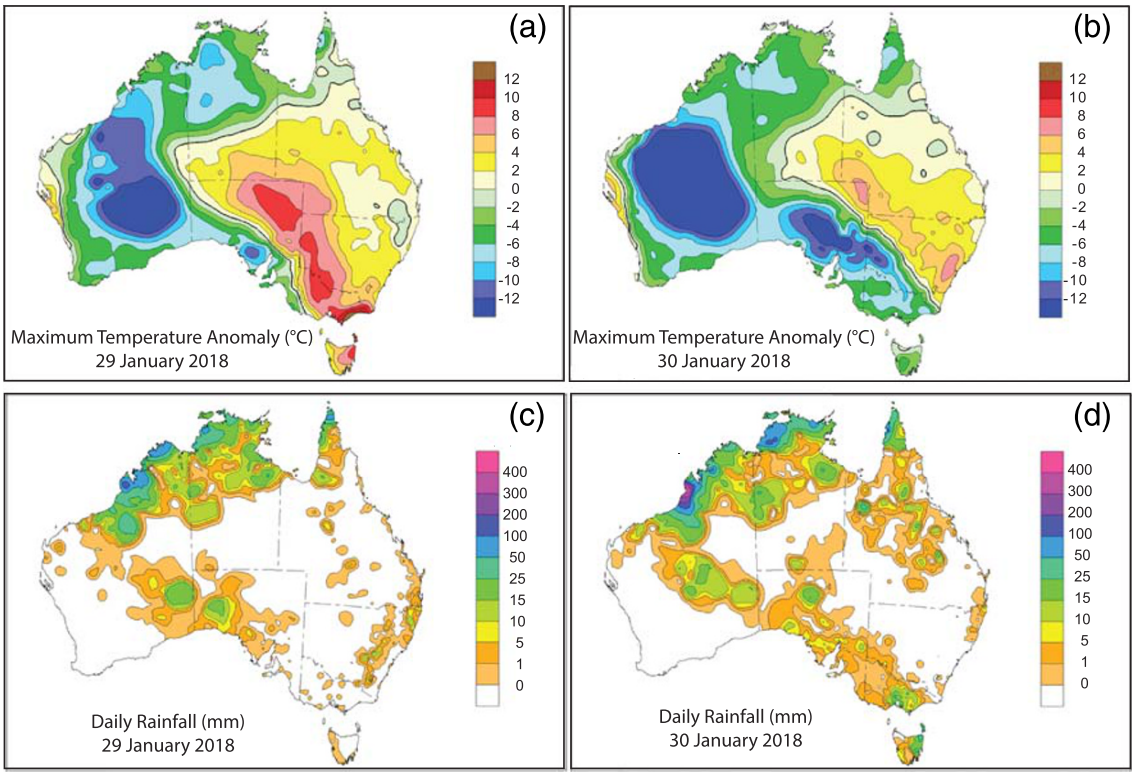

Figure 5. Maximum temperature anomaly (°C) on (a) 29 January 2018 local time (1300 28 January to 1300 29 January UTC) and (b) 30 January 2018 LT. Twenty-four hour rainfall (mm) on (c) 29 January 2018 LT and (d) 30 January 2018 LT across the continent of Australia (©Commonwealth of Australia, Bureau of Meteorology, used under Creative Commons Attribution License https://creativecommons.org/licenses/by/3.0/au/).

5,500 m. Dropsondes were launched at 0008, 0025, 0043, 0101, and 0119 UTC southwest of the AR over boundary layer clouds (Figure 2). The G-V sampled Southern Ocean boundary layer clouds during the principal part of the mission; upon return, the AR was still located over Hobart. The G-V thus climbed to 8,000 m prior to entering the AR and dropped three sondes at 0457, 0516, and 0531 UTC while crossing the western half of the AR (Figure 2). The aircraft then descended through the AR, landing at Hobart airport.

2.2. Satellite Data and Imagery

Enhanced infrared (Channel 13, 10.4-μm wavelength band) geostationary satellite images over Australia and the Southern Ocean used in this paper were produced by NCAR using data from the Japan Meteorological Agency's Himawari 8 satellite. Satellite rainfall data were obtained from the National Aeronautics and Space Administration (NASA) Global Precipitation Measurement (GPM) mission Integrated Multi-satellite Retrievals (IMERG) version 05B, Final Run (Huffman et al., 2018). Between 60°N/S latitude, IMERG uses global geostationary infrared brightness temperatures to advect passive microwave-retrieved precipitation estimates available from a constellation of low-Earth orbit satellites. Once precipitation system motion is estimated from National Oceanographic and Atmospheric Administration (NOAA) Climate Prediction Center (CPC) 30-min 4-km globally stitched infrared images (Joyce et al., 2001), advection is performed with an ensemble Kalman filter technique (Joyce et al., 2011). Poleward of 60°N/S latitude, the infrared advection is not used, and precipitation estimates are only available during microwave passes. The final estimates are calibrated to available Deutscher Wetterdienst (DWD) Global Precipitation Climatology Center (GPCC) global gauge measurements on a monthly time scale. The product used in this study has 30-min temporal and 0.1° latitude-longitude spatial resolution.

3. Model Simulation

A water vapor tracer-enabled version of the WRF model is used to quantify the contribution of tropical moisture. WRF with water vapor tracers (WRF-WVT; Insua-Costa & Miguez-Macho, 2018), unlike

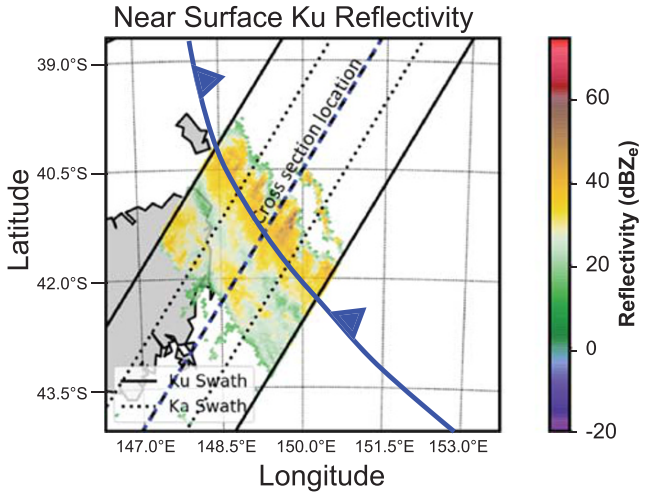

Figure 6. Global precipitation mission (GPM) near-surface Ku band equivalent radar reflectivity factor across atmospheric river just east of Tasmania, Australia, at 1908 UTC 29 January 2018 along GPM orbit 022280. Surface cold frontal position based on ERA-Interim analysis of surface wind and temperature field at 1800 UTC 29 January 2018.

traditional WRF, uses an extra WVT module to numerically "tag" moisture of a specific origin and track its life cycle in the atmosphere until it falls out as precipitation. WVT is analogous to putting "dye" in the model's hydrologic cycle (Sodemann et al., 2008) and has been implemented in climate models (e.g., Bosilovich & Schubert, 2002; Goessling & Reick, 2012; Nusbaumer & Noone, 2018; Sodemann et al., 2008) to diagnose moisture sources and pathways. In this study, WVT is used to "tag" moisture from the tropics (here defined as latitudes equatorward of 25°S) as tracer moisture. This WVT module calculates its transport and phase change processes enabling a full consideration of physical processes for atmospheric moisture represented in the WRF model such as advection, diffusion, convection, and cloud microphysical processes (see more details in Insua-Costa & Miguez-Macho, 2018). As a result, a quantitative estimate of moisture contribution from the tropics to the total moisture field and precipitation is obtained.

Figure 3 shows the simulation domain covering the AR's extension over Australia and the Southern Ocean with a 20-km grid spacing. The simulation used 40 vertical levels from the surface to 50 hPa. ERA-Interim Reanalysis (T255 spectral, 60 levels in the vertical from the surface up to 0.1 hPa, 0.75° spatial resolution, and 6-hourly resolution; Dee et al., 2011) is used as the initial and boundary conditions to drive the WRF-WVT simulation. The model is initialized at 0000 UTC 15 January and is run for 17 days until 0000 UTC 1 February. The simulation is initialized ~14 days before the mature stage of this AR (14 January) in order to capture tropical-originated moisture that exists in the midlatitudes with residence times up to 14 days. The physical parameterization schemes used are the Yonsei University planetary boundary layer (YSU PBL) scheme (Hong & Pan, 1996), the Kain-Fritsch (Kain, 2004), and the WSM6 microphysics scheme (Hong & Lim, 2006). Spectral nudging every 6 hr constrains the synoptic scales to follow the reanalysis (Miguez-Macho et al., 2004). The WVT module tags the moisture in the tropics as tracer moisture at each model time step, with an initial field of the ratio of tracer moisture to total moisture that continuously evolves.

4. AR Characteristics

The AR developed over Australia and the Southern Ocean as the Australian monsoon trough and associated ITCZ thunderstorms occurred along the northern coast of the continent (Figure 1). Moisture feeding into the AR from the tropics originated near a warm core tropical depression within the monsoon trough, centered over land at 20°S and 125°E, and evident as a 1,350-m depression in the 850-hPa height field between 0000 UTC 28 January and 1200 UTC 30 January (Figures 4a–4f). An animation of Himawari 8 geostationary images of the region showed convection erupting within the depression as the system rotated cyclonically,

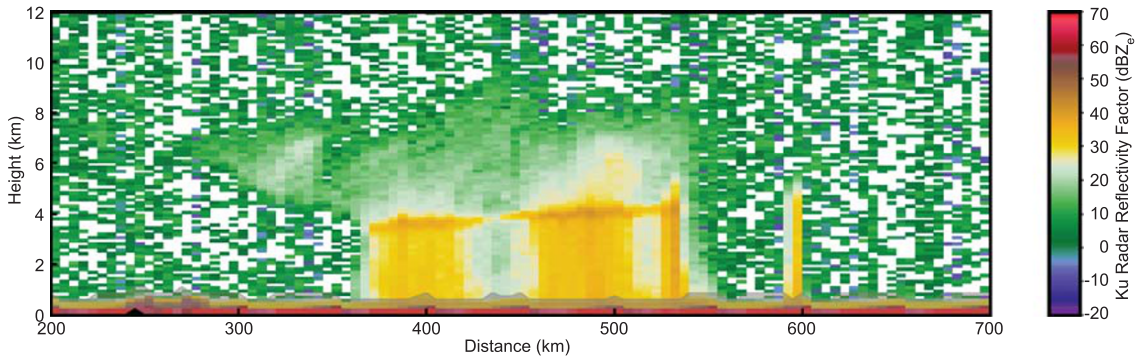

Figure 7. Cross section along blue dashed line in Figure 6 showing near-surface Ku band reflectivity factor (dBZ_e) measured during an overpass of the atmospheric river by the GPM satellite.

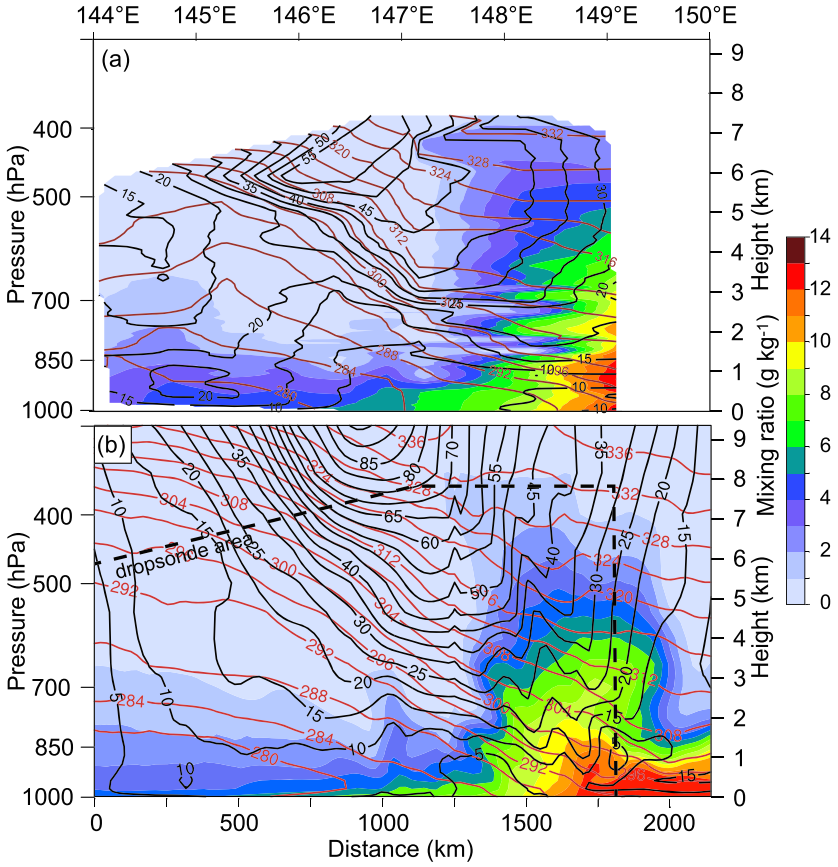

Figure 8. (a) Dropsonde and (b) model cross sections showing water vapor mixing ratio (colors) potential temperature (red/brown contours, K) and wind speed normal to the cross section (black contours, m s^{-1}). The model cross section is parallel to the dropsonde launch pattern (Figure 2).

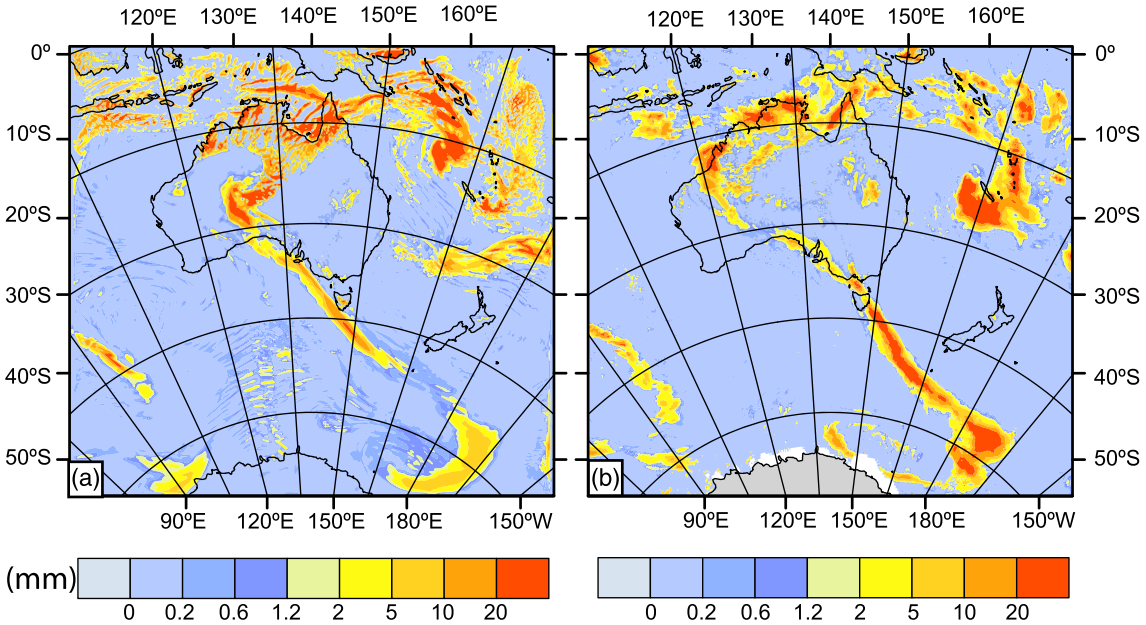

Figure 9. (a) WRF simulated precipitation (mm) and (b) GPM estimated precipitation (mm) for the period 0300–0900 UTC 29 January 2018.

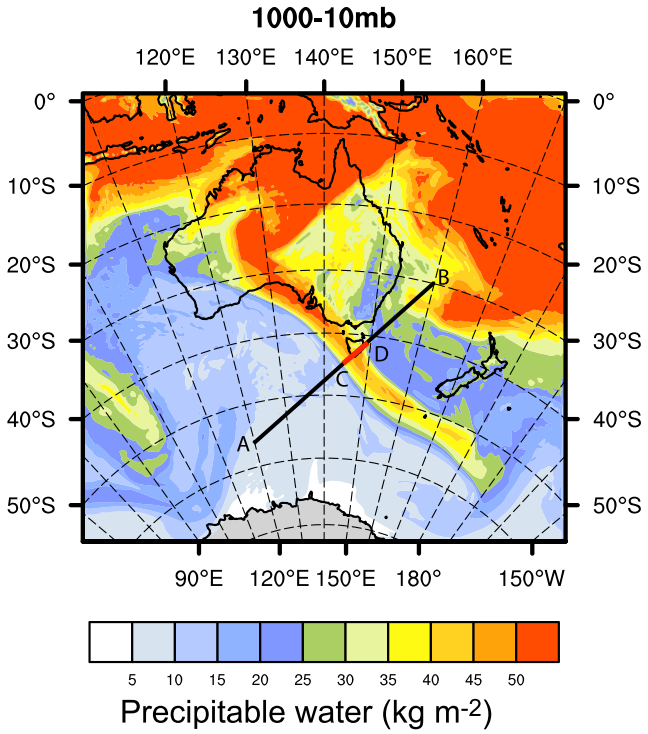

Figure 10. Precipitable water (kg m^{-2}) at 0600 UTC 29 January 2018 from the WRF simulation. Cross sections along line A–B appear in Figures 12 and 13.

with cloud elements from convection entering the AR and flowing southeastward along it (see supporting information). The AR extended southeastward 3,300 km across the deserts of Western Australia and along the southern coast to Tasmania, before emerging over the Southern Ocean. The IVT dropped to 50–350 kg m^{-1} s^{-1} over Western Australia deserts as precipitation occurred (Figures 5c and 5d) and there was no surface source of moisture to replenish the AR. The core again exceeded 500 kg m^{-1} s^{-1} south of the southern coast of Australia. From Tasmania, the AR extended 2,700 km further southeastward to 55°S and 180°E over the Southern Ocean. At this latitude, the IVT dropped below 500 kg m^{-1} s^{-1} (Figures 4a–4f) and the cloud field associated with the AR could not be distinguished on visible satellite imagery from other clouds (Figure 1a). The width of the AR cloud field across Australia and the Southern Ocean was approximately 500 km. The time series of IVT in Figures 4a–4f between 0000 28 January through 1200 UTC 30 January 2018 shows that IVT through the core of the AR exceeded 500 kg m^{-1} s^{-1} throughout this period. The IVT was along the east side of a trough that extended from Australia to Antarctica (see 850- and 300-hPa height field in Figures 4a–4l). Winds within the upper-level jet stream over the front exceeded 55 m s^{-1} (Figures 4g–4l). Dropsonde measurements (see section 5) showed winds in excess of 40 m s^{-1} extending downward to 3.5 km and 20 m s^{-1} to 2 km above mean sea level (MSL).

The AR flowed on the warm side of, and parallel to, a strong cold front (see section 6) that extended northward from a surface cyclone located just north of Victoria Land, Antarctica, at 60°S and 155°E over the Southern Ocean, and west of a high-pressure system around 170°E and 40°S over New Zealand (Figures 4a–4f). These features are characteristic of ARs (American Meteorological Society, 2020; Ralph et al., 2018) including those affecting Antarctica (Gorodetskaya et al., 2014). At 0000 UTC 29 January, the AR crossed the Australian coast just west of Tasmania. A 55–85 m s^{-1} southwesterly jet stream was present at 300 hPa, coincident with the AR over the Southern Ocean (Figures 4g–4l). Over southern Australia, a sharp thermal gradient was present at the surface associated with the cold front (Figures 5a and 5b). Precipitation from the AR fell in a band across the western desert as well as the southcentral and southeastern coast, with local 24-hr precipitation accumulations ranging from 1 to 24 mm, as measured by the Australian Bureau of Meteorology (Figures 5c and 5d). The 24-hr precipitation associated with this AR was compared to the climatological mean of daily values for December–February. Along the path of the AR, local 24-hr precipitation values well exceeded the climatological mean everywhere across Australia.

A GPM satellite overpass of the AR occurred at 1908 UTC 29 January when the AR was along and off the east coast of Tasmania (Figure 6). At that time, the AR was associated with two linear precipitation bands parallel to the cold front (Figure 7). Two-banded structure was also observed 14 hr earlier with the airborne W-Band radar when the G-V crossed the AR on its approach to Hobart. The dropsondes showed that the westernmost narrower band was located directly along the cold front, while the eastern band was prefrontal (Part II).

5. Comparison of the Model Simulation With Observations

The model simulated frontal structure was compared directly with thermodynamic and wind measurements made with dropsondes during the flight, with GPM measurements of precipitation over the Southern Ocean, and with satellite estimates of precipitable water along its length. Figure 8a shows a cross section of potential temperature (θ), wind speed normal to the cross section (v), and mixing ratio (q) constructed from measurements from the eight dropsondes launched between the times of 0008 UTC and 0531 UTC, and Figure 8b shows a corresponding model cross section at 0500 UTC aligned with the dropsonde curtain (see Figure 2). The time 0500 UTC was used because the three dropsondes closest to and within the AR bridged this time (Figure 2). Although the simulation reproduced essential features of the frontal

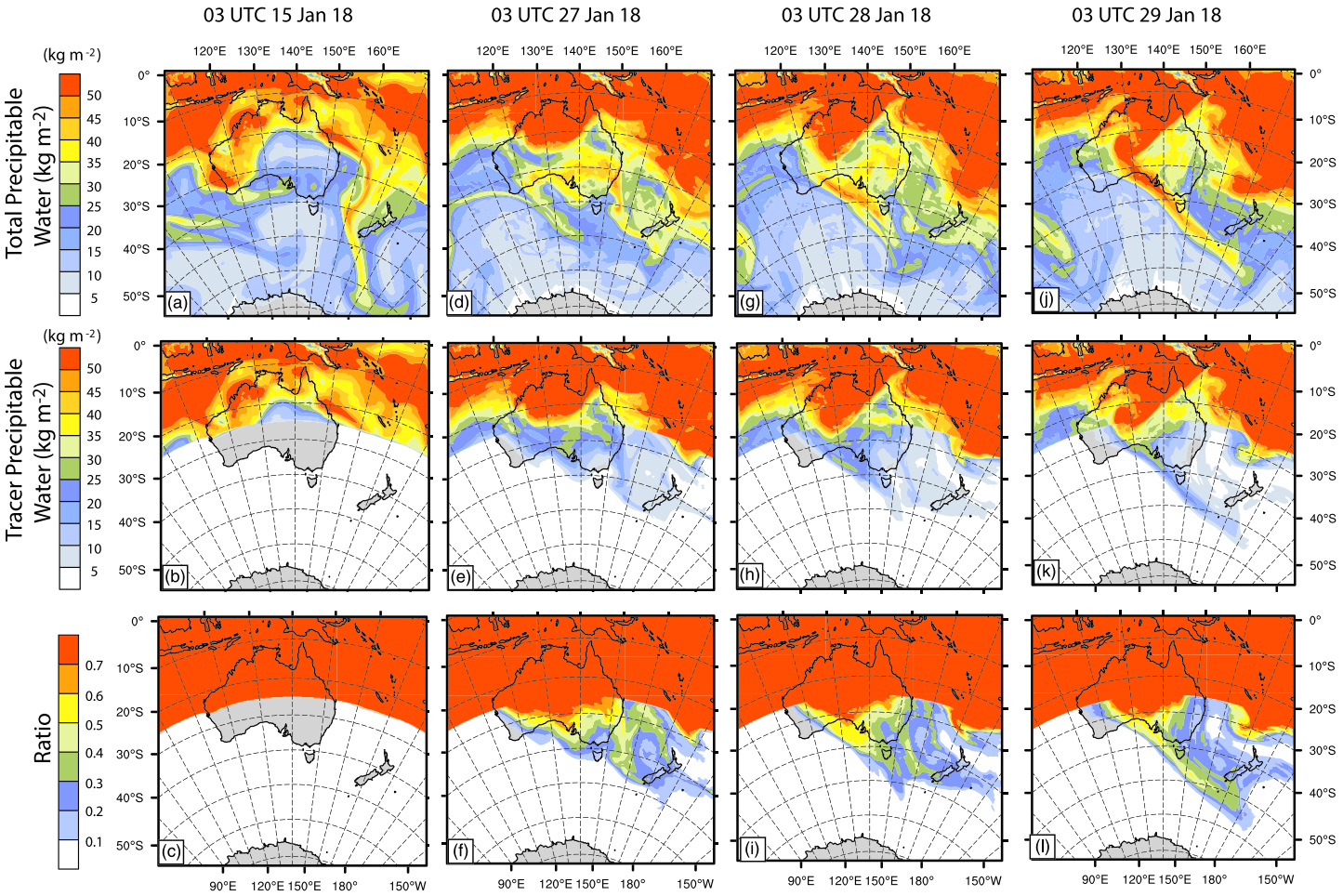

Figure 11. Evolution of the simulated precipitable water (kg m^{-2}) from the beginning of the model simulation at 0300 UTC 15 January through 0300 UTC on 27, 28, and 29 January 2018: top row (a, d, g, l): total precipitable water; (b) middle row (b, e, h, k): precipitable water originating north of 25°S latitude only; and (c) bottom row (c, f, i, l) the ratio of tropical-contributed precipitable water to the total precipitable water.

zone, the midtropospheric (3–6 km) observed frontal slope was somewhat steeper (7.5 m km^{-1} observed vs. 5.3 m km^{-1} modeled), and the midtropospheric temperature gradient was somewhat greater (4.1 K/100 km vs. 2.8 K/100 km at 4-km altitude), but the magnitude and vertical and horizontal distribution of the water vapor mixing ratio was very similar (e.g., 12–13 g kg^{-1} near the surface, reducing to 6–7 g kg^{-1} at 4 km just east of the front). The strength of the central jet stream over the front at 7-km altitude was overestimated by about 10 m s^{-1} in the simulation.

Precipitation was determined from the GPM constellation from 0300 to 0900 UTC using the method described in section 2.2 (Figure 9b). Precipitation was also integrated from the model during the same period (Figure 9a). Although both show the AR as a distinct feature over Australia and the Southern Ocean, the location of the AR precipitation in the model simulation lagged westward from that in the GPM estimate by approximately 200 km near Tasmania, and less so over the Southern Ocean, implying that the eastward frontal movement in the model was not as fast as occurred in nature. The model precipitation and GPM estimates also varied with location along the AR. The largest disagreement occurred in two areas, the first directly south of New Zealand, where the model produced precipitation of 1–2 versus 10–20 mm in the GPM estimate, and within the monsoon trough near the north end of the AR, where the distribution of convective precipitation was concentrated on the southern side of the depression in the model versus the north side in the observations. The greatest agreement between the model and GPM estimates occurred along the south Australia coastline to south of Tasmania, where the values for precipitation ranged from 5 to 20 mm,

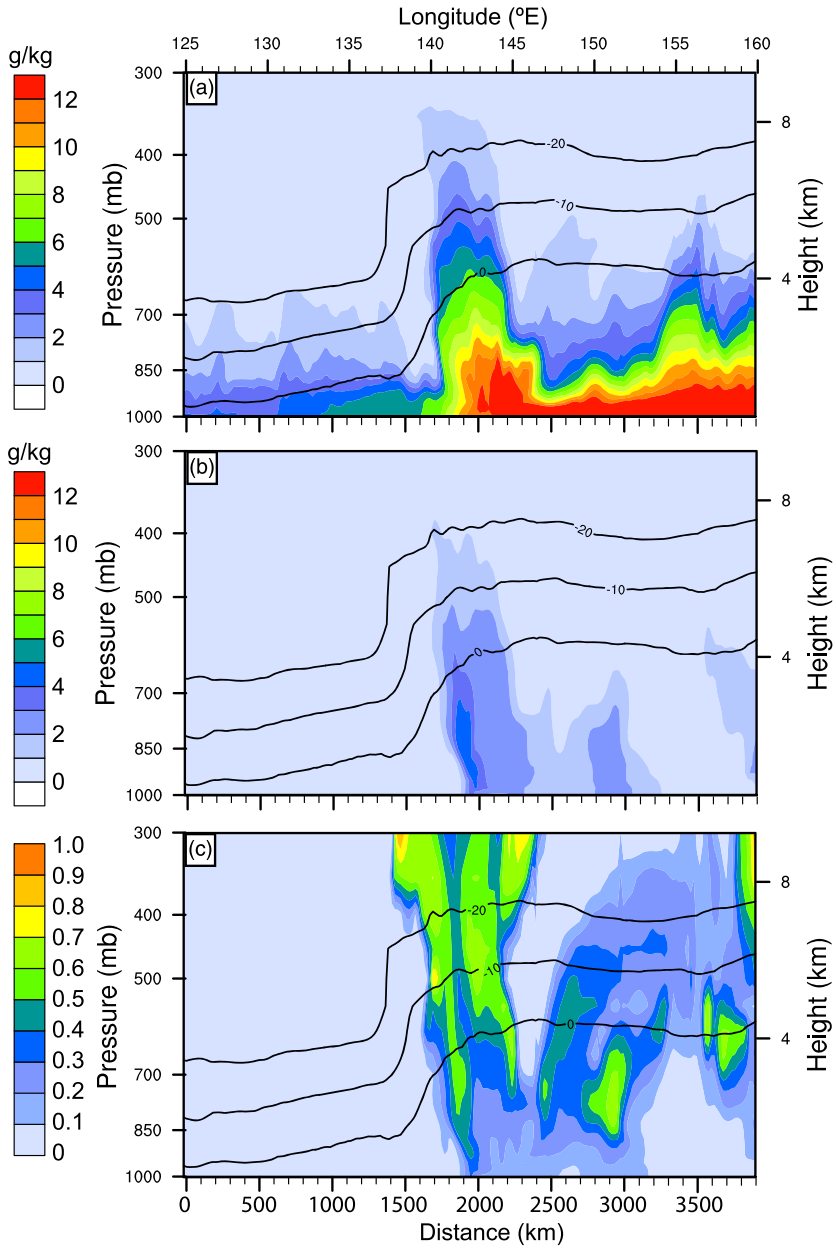

Figure 12. Vertical distribution of moisture at 0600 UTC along cross section A–B in Figure 10: (a) total mixing ratio (g kg^{-1}); (b) mixing ratio associated with "tagged" tropical moisture (g kg^{-1}); and (c) the ratio of tropical-contributed moisture to the total moisture (b divided by a). Black lines are isotherms (°C).

although the areal coverage of heavier precipitation across the AR in the GPM estimate was greater than that calculated in the simulation.

Figure 10 shows the simulated precipitable water at 0600 UTC 29 January, near the time when the G-V aircraft was flying through the AR on its return from the Southern Ocean. The precipitable water vapor associated with the AR appears as a distinct feature across Australia and the Southern Ocean. Comparing Figure 10 with Figure 1b, over northern tropical Australia, precipitable water values were similar, 50–60 kg m^{-2}. Over Central Australia, the model maintained these values while the data show a reduction to 30–40 kg m^{-2}, likely due to precipitation over the central desert areas (Figures 5c and 5d). South of Central Australia, in the model values were 55 kg m^{-2} near the Australian coast, decreasing with distance to

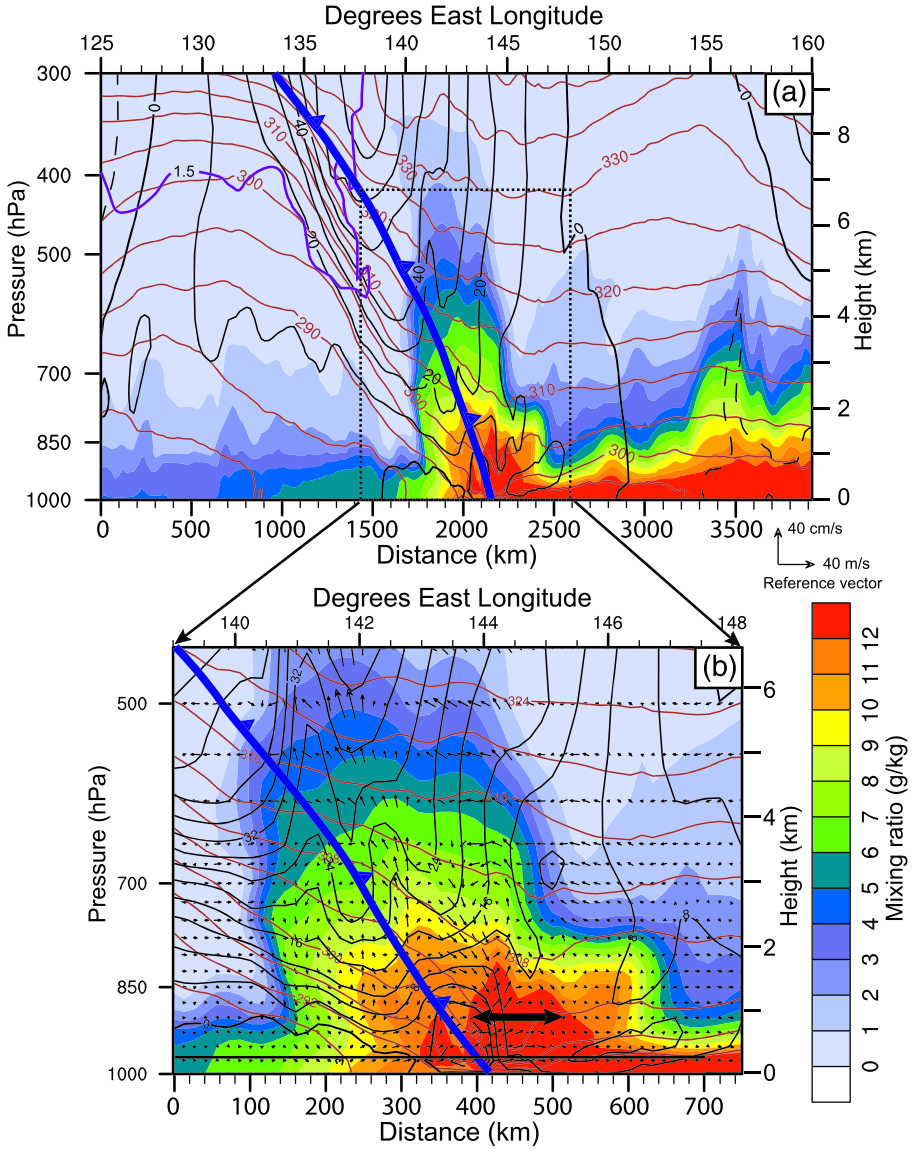

Figure 13. (a) Model cross section at 0600 UTC 29 January along line A–B in Figure 10 showing potential temperature (brown, K), wind speed normal to the cross section (black, m s^{-1}), the 1.5 PVU isentropic potential vorticity contour (purple, 10^{-6} m^2 s^{-1} K kg^{-1}), the mixing ratio (g kg^{-1}, colors), and the cold front; (b) expansion of the dashed boxed area in (a) showing potential temperature, wind normal to the cross section, mixing ratio, and the ageostrophic circulation (see vector scale on right between a and b). The horizontal black arrow in (b) denotes the region where the vertical water vapor flux in Figure 14 was calculated.

35 kg m^{-2} over the Southern Ocean south of 50°S. These values can be compared with satellite-based estimates which ranged from 60 kg m^{-2} near the coast to ~35 kg m^{-2} near 50°S (Figure 1b).

6. Tropical Versus Midlatitude Moisture Sources

The moisture tracer technique described in section 3 was applied throughout the simulation to isolate moisture originating within the monsoon trough north of 25°S from that originating south over the midlatitudes. Figure 11a shows the initial state of the precipitable water field across the model domain at 0300 UTC 15 January, tropical precipitable water in Figure 11b, and their ratio in Figure 11c. In the ensuing 12-day period through 0300 UTC 27 January, before the development of the AR, some intrusion of tropical moisture over southern Australia occurred as a result of migrating fronts, but the signature of the AR only became

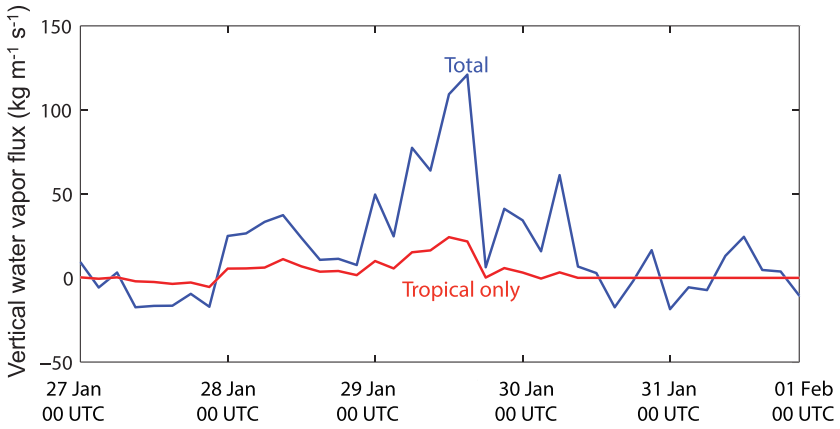

Figure 14. Time series of vertical water vapor flux integrated over the region indicated by the horizontal arrow at 900 hPa in Figure 13b. Blue is the total water vapor flux, and red is the tracer vapor flux sourced from the tropics.

apparent 48 hr before the flight (Figures 11d–11f). The impact of the cold front and associated AR on the distribution of moisture progressively became more apparent over the next 48 hr (Figures 11g–11l). The tropical contribution to the AR during this period is best quantified in terms of the ratio field in Figures 11i and 11l. South of the Australia coast, 30–60% of the precipitable water within the AR originated in the tropics. The vertical distribution of the total moisture, tropical moisture, and their ratio at 0600 UTC 29 January at the latitude of Tasmania (Figure 12) shows that the tropical moisture was distributed through the vertical column as the flow moved out over the Southern Ocean (Figure 12b). However, the model results also show that as much as 50–60% of the moisture within the AR at altitudes *above* the 0°C isotherm was tropical in origin at the time the aircraft sampled the pre-cold frontal zone (Figure 12c). The results imply that tropical moisture was lofted into the middle and upper troposphere in connection with tropical convection and was then transported into midlatitudes along the jet stream. Although the mixing ratio associated with tropical moisture was 2 g kg^{-1} or less above the 0°C isotherm, 50 to 60% of that moisture originated in tropical latitudes. This result implies that a large fraction of the water mass of ice particles falling through the melting level to form raindrops originated north of 25°S.

The primary source of water mass below the 0°C isotherm was determined by examining the ageostrophic circulation about the frontal zone. Figure 13a shows a 3,900 km long cross section normal to the AR at the latitude of Tasmania through the modeled front (line A–B on Figure 10) and an expanded region near the front (Figure 13b) detailing the ageostrophic circulation. In Figure 13b, the components of the ageostrophic circulation vectors are the vertical velocity and the component of the ageostrophic wind parallel to the cross-sectional plane. The cold frontal zone associated with this AR extended through the depth of the troposphere. The 1.5 isentropic potential vorticity contour extended downward to 550 hPa within the frontal zone, indicative of ageostrophically forced descent of stratospheric air. On the warm side of the front, the ageostrophic circulation produced upward motion that increased with altitude from a few cm s^{-1} near 800 hPa to approximately 0.5 m s^{-1} near the top of the precipitation band and just below the jet stream level at 420 hPa. At altitudes below 800 hPa, weak downdrafts (see ageostrophic circulation vectors) were present ahead of the front, coincident with the precipitation region. A 70 m s^{-1} jet stream was present over the front in the upper troposphere. A low-level jet feature, commonly observed in north Pacific ARs (e.g., Neiman, Ralph, Wick, Kuo, et al., 2008; Ralph et al., 2011), was present in the simulation, but had a smaller range of magnitudes (10–20 m s^{-1}) than typically observed over the north Pacific, where composite values ranged from 15.9 to 28.5 m s^{-1} during the PACJET and CALJET studies, respectively (Ralph et al., 2005). Another difference between this AR and north Pacific ARs was the height of the melting level. Since this AR occurred in the austral summer, the melting level was near 4 km on the warm side of the front (see radar bright band in Figure 7). In wintertime north Pacific ARs impacting the Sierra Nevada, the melting layer normally varies between 800 and 2,800 m (Lundquist et al., 2008). At the latitude of Tasmania, near-surface mixing ratios ahead of the front were ~12 g kg^{-1}, higher than the composite 9 g kg^{-1} reported by Ralph et al. (2005) for north Pacific ARs. Figure 13a also shows that most of the moisture within the AR resided below the 0°C

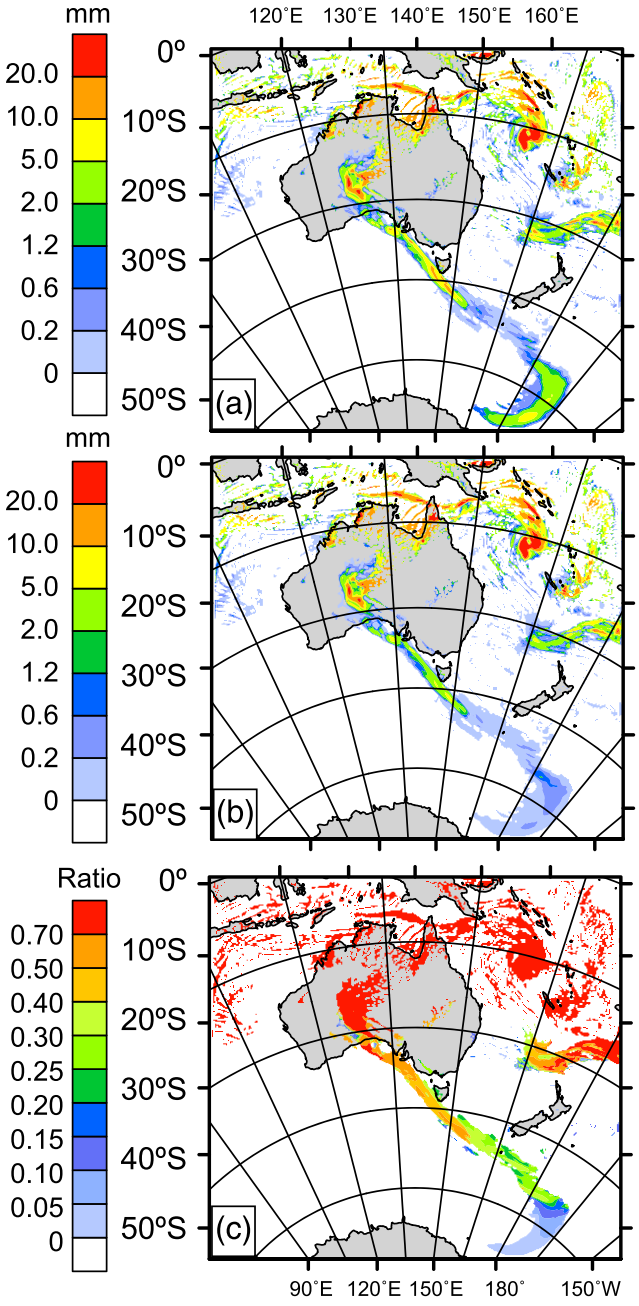

Figure 15. Simulated precipitation (mm) integrated from 0300 UTC 29 January 18 to 0600 UTC, 29 January: (a) total precipitation; (b) precipitation due to "tagged" tropical moisture; and (c) the ratio of tropical-contributed precipitation to total precipitation (b divided by a).

isotherm. This region represents the zone where raindrops forming at the melting level continue growth to cloud base through collision and coalescence with cloud droplets (see Part II).

The distribution of moisture in the vicinity of the front together with the ageostrophic circulation vectors suggests that surface-based moisture was transported upward into the AR as a result of the ageostrophic circulation about the front and lifting directly at the frontal boundary. The role of the ageostrophic circulation in supplying low level moisture to the AR was determined quantitatively by calculating the vertical moisture flux through the 900 hPa level along cross section C–D in Figure 10 (see also bold horizontal arrow in Figure 13b). An upward moisture flux associated with the frontal passage first became apparent at 0000 UTC 28 January as the front approached, increasing to a peak value of 130 kg m^{-1} s^{-1} at 1200 UTC 29 January during the time the clouds associated with the front moved across Tasmania (Figure 14). The upward flux of tropical moisture through the 900 hPa level was small, peaking at 23 kg m^{-2} s^{-1}, approximately 18% of the total flux. These results, together with Figures 12a and 12b, suggest that most of the moisture below the altitude of the 0°C isotherm was locally sourced at the time when the AR crossed over the southern Australia coast.

The contribution of tropical moisture to precipitation over the Southern Ocean within the AR between 0300 and 0600 UTC 29 January appears in Figures 15a–15c. Over Australia, over 70% of the precipitation was related to tropical moisture. About 50% of the simulated AR precipitation directly south of Australia was of tropical origin. This contribution diminished southward of 45°S to less than 5% at 55°S, suggesting an increasing role of local oceanic moisture on precipitation at higher latitudes approaching Antarctica. Notably, the pre-cold frontal zone from southern Australia to 45°S shows similar contributions from tropical moisture to precipitable water (Figure 11l) and precipitation, implying an efficient mixing of the vapor within the column to form precipitation (Figure 15c).

The full impact of the AR on the transport of tropical moisture over the Southern Ocean was assessed along cross section C–D in Figure 10 by computing the time evolution of the vertically IWV flux, calculated as in Guan et al. (2018), across the 500-km width of the AR throughout its 5-day lifetime (Figure 16). Tropical moisture accounted for approximately 50% of the total flux in peak flux hours from 1200 UTC 28 January to 1200 UTC 29 January. The peak flux was approximately 3.5 times the climatological value for the summer months of December–February (Figure 16). In terms of strength, the IVT through the core of this AR (C–D in Figure 10) reaches above 500 kg m^{-1} s^{-1} during 1200 UTC 28 January to 0600 UTC 29 January 29. This is a strong AR in comparison with all the ARs that occur globally, which, by estimation of Guan and Waliser (2015), have a median IVT value of 374 kg m^{-1} s^{-1}. This high IVT strength might be attributed to the higher water vapor content associated with the warmer temperatures in austral summer in contrast to winter ARs that have been studied in the Northern Hemisphere and are characterized by strong winds (e.g., Ralph et al., 2004, 2011). The integrated total water vapor passing through the AR during the two most intense days (28 and 29 January) was 4.5×10^{13} kg, of which 2.0×10^{13} kg was tropical moisture. The integrated total water vapor passing through the AR during the entire 5-day period represented on Figure 16 was 6.5×10^{13} kg with 2.6×10^{13} kg from the tropics. For

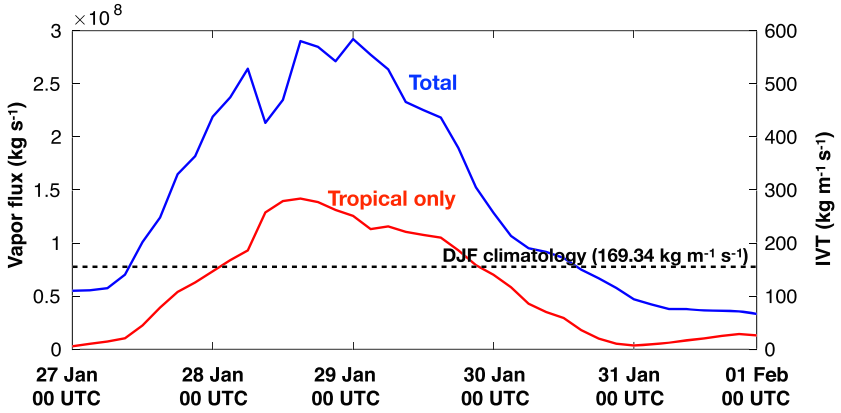

Figure 16. Total and tropical mass flux of water vapor over 5 days within atmospheric river integrated from C to D in Figure 10. The December–February climatological value of IVT across the similar location is also shown (black dashed line; between 145°E and 150°E at 43.5°S).

perspective, the average flux of water discharge of the Amazon River is 2.0×10^8 kg s^{-1}. In 2 days, the Amazon discharges 3.5×10^{13} kg. The moisture passing through the AR at Tasmania during the two most intense days was 1.3 times the Amazon discharge. Forty-four percent of that water was sourced from latitudes north of 25°S.

7. Summary and Conclusions

This paper together with Part II are the first to analyze an AR event impacting Tasmania, Australia, and the Southern Ocean region using both a modeling and observational approach. The studies resulted from an unanticipated opportunity to observe the structure and microphysics of an AR event over the region that occurred during the SOCRATES campaign on 28 and 29 January 2018. In this paper, Gulfstream-V dropsonde measurements and GPM precipitation and radar analyses were used in conjunction with WRF simulations with water vapor tracers to investigate the relative contributions of tropical and midlatitude moisture sources to the AR. The dropsonde measurements confirmed that the model captured the details of the frontal structure. The GPM measurements and comparison with satellite-estimated precipitable water showed that the model underestimated the precipitation in the AR. The frontal movement in the model was not as fast as occurred in nature, and precipitation structures were displaced westward, but overall, the simulation was sufficiently robust that the following conclusions could be drawn.

1. Moisture associated with a monsoonal tropical depression over Western Australia brought precipitation and cooler temperatures along the AR path extending through the Western Australian continent out and over the Southern Ocean to latitudes south of 60°S.
2. The enhanced tropical moisture became entrained into a midlatitude frontal system that extended far into the Southern Ocean reaching the associated low-pressure system off the east coast of Antarctica—effectively connecting the tropics and polar latitudes.
3. Using WRF-WVT, it was shown that south of the Australian coast, tropical moisture contributed up to 50% of the precipitable water within the AR. The tropical moisture contribution to precipitation decreased with latitude, from >70% over the Australian continent, to ~50% off the Australian coast, to less than 10% poleward of 60°S
4. Some of the important contrasts between this AR and the much more thoroughly studied Northern Hemisphere ARs include the fact that this very strong system occurred in the summer (as opposed to the more typical strong winter events in the Northern Hemisphere). The tendency to occur in summer may be related to the summertime presence of the monsoon trough over northern Australia, which can become a source of tropical moisture. The tropical moisture crossed the arid regions of Western Australia before becoming entrained in the extratropical system—while most other ARs develop over oceanic regions and then impinge into the continents.
5. In terms of the strength, the IVT through the core of this AR (C–D in Figure 10) was above 500 kg m^{-1} s^{-1} during 1200 UTC 28 January to 0600 UTC 29 January 29, reaching a maximum IVT value of 600 kg m^{-1} s^{-1}

(Figure 16). This is an above-average AR in comparison with the global climatological IVT value for ARs of 374 kg m^{-1} s^{-1} (Guan & Waliser, 2015). Compared to other ARs in this part of the world, this AR is about average in terms of total IVT (Guan et al., 2018). When using the AR scale developed by Ralph et al. (2019), this AR would be classified as a Cat 2—mostly beneficial but also potentially hazardous. Integrating IVT over the width of this AR (~500 km from C to D in Figure 10), water volume transport occurred at a similar rate as the Amazon River discharge (2.0×10^8 kg s^{-1}), lasting ~2 days in this AR's lifetime, half of which was transported from the tropics. This value is of the same order of magnitude as dropsonde IVT estimates in Northern Hemisphere Pacific Ocean ARs (Guan et al., 2018; Ralph et al., 2017).

6. Tropical moisture in this event contributed 50–60% of the moisture above the 4-km level, which corresponded to the height of the 0°C isotherm as the AR emerged over the Southern Ocean at Tasmania. At altitudes below the 0°C isotherm, moisture was largely of midlatitude origin.

In Part II of this series, we investigate characteristics of ice particles formed aloft within the tropical moisture plume and how ice particles effectively initiated collision-coalescence and precipitation growth though warm rain processes as they descended through the melting level of the AR.

Data Availability Statement

Dropsonde data (https://doi.org/10.5065/D6QZ28SG), NASA SatCORPS Himawari Cloud retrieval data (https://doi.org/10.5065/D6CC0ZFJ), GPM-DPR data (https://doi.org/10.5067/GPM/DPR/GPM/2A/05), and GPM IMERG data (https://doi.org/10.5067/GPM/IMERG/3B-HH/05) that support the findings of this study are available and accessible online.

Acknowledgments
This work was supported by the National Science Foundation (grants AGS 1628674 and 1762096) and National Aeronautics and Space Administration (grant 80NSSC19K0713). We appreciate the efforts of the entire SOCRATES team in collecting a high-quality data set.

References

American Meteorological Society (2020). "Atmospheric river". Glossary of Meteorology. Available online at http://glossary.ametsoc.org/wiki/Atmospheric_river

Bao, J., Michelson, S. A., Neiman, P. J., Ralph, F. M., & Wilczak, J. M. (2006). Interpretation of enhanced integrated water vapor bands associated with extratropical cyclones: Their formation and connection to tropical moisture. *Monthly Weather Review*, *134*(4), 1063–1080. https://doi.org/10.1175/MWR3123.1

Bosilovich, M., & Schubert, S. (2002). Water vapor tracers as diagnostics of the regional hydrologic cycle. *Journal of Hydrometeorology*, *3*(2), 149–165. https://doi.org/10.1175/1525-7541(2002)003<0149:WVTADO>2.0.CO;2

Bozkurt, D., Rondanelli, R., Marín, J. C., & Garreaud, R. (2018). Foehn event triggered by an atmospheric river underlies record-setting temperature along continental Antarctica. *Journal of Geophysical Research: Atmospheres*, *123*, 3871–3892. https://doi.org/10.1002/2017JD027796

Cannon, F., Cordeira, J. M., Hecht, C. W., Norris, J. R., Michaelis, A., Demirdjian, R., & Ralph, F. M. (2020). GPM satellite radar observations of precipitation mechanisms in atmospheric rivers. *Monthly Weather Review*, *148*(4), 1449–1463. https://doi.org/10.1175/MWR-D-19-0278.1

Cordeira, J. M., Ralph, F. M., & Moore, B. J. (2013). The development and evolution of two atmospheric rivers in proximity to western north Pacific tropical cyclones in October 2010. *Monthly Weather Review*, *141*(12), 4234–4255. https://doi.org/10.1175/MWR-D-13-00019.1

Dacre, H. F., Clark, P. A., Martinez-Alvarado, O., Stringer, M. A., & Lavers, D. A. (2015). How do atmospheric rivers form? *Bulletin of the American Meteorological Society*, *96*(8), 1243–1255. https://doi.org/10.1175/BAMS-D-14-00031.1

Dee, D. P., Uppala, S. M., Simmons, A. J., Berrisford, P., Poli, P., Kobayashi, S., et al. (2011). The ERA-Interim reanalysis: Configuration and performance of the data assimilation system. *Quarterly Journal of the Royal Meteorological Society*, *137*(656), 553–597. https://doi.org/10.1002/qj.828

Dettinger, M. D., Ralph, F. M., Das, T., Neiman, P. J., & Cayan, D. R. (2011). Atmospheric rivers, floods, and the water resources of California. *Water*, *3*(2), 445–478. https://doi.org/10.3390/w3020445

Dominguez, F., Hu, H., & Martinez, J. A. (2020). Two-layer dynamic recycling model (2L-DRM): Learning from moisture tracking models of different complexity. *Journal of Hydrometeorology*, *21*(1), 3–16. https://doi.org/10.1175/JHM-D-19-0101.1

Eiras Barca, J., Dominguez, F., Hu, H., Garaboa Paz, D., & Miguez-Macho, G. (2017). Evaluation of the moisture sources in two extreme landfalling atmospheric river events using an Eulerian WRF tracers tool. *Earth System Dynamics*, *8*(4), 1247–1261. https://doi.org/10.5194/esd-8-1247-2017

Finlon, J. A., Rauber, R. M., Wu, W., Zaremba, T. J., McFarquhar, G. M., Nesbitt, S. W., et al. (2020). Structure of an atmospheric river over Australia and the Southern Ocean. Part II: Microphysical evolution. *Journal of Geophysical Research: Atmospheres*, *125*, e2020JD032514. https://doi.org/10.1029/2020JD032514

Gimeno, L., Dominguez, F., Nieto, R., Trigo, R., Drumond, A., Reason, C. J. C., et al. (2016). Major mechanisms of atmospheric moisture transport and their role in extreme precipitation events. *Annual Review of Environment and Resources*, *41*(1), 117–141. https://doi.org/10.1146/annurev-environ-110615-085558

Gimeno, L., Stohl, A., Trigo, R. M., Dominguez, F., Yoshimura, K., Yu, L., et al. (2012). Oceanic and terrestrial sources of continental precipitation. *Reviews of Geophysics*, *50*, RG4003. https://doi.org/10.1029/2012RG000389

Goessling, H. F., & Reick, C. H. (2012). Atmospheric water vapour tracers and the significance of the vertical dimension. *Atmospheric Chemistry and Physics Discussions*, *12*(11), 30,119–30,176. https://doi.org/10.5194/acpd-12-30119-2012

Gorodetskaya, I. V., Silva, T., Schmithüsen, H., & Hirasawa, N. (2020). Atmospheric river signatures in radiosonde profiles and reanalyses at the Dronning Maud Land coast, East Antarctica. *Advances in Atmospheric Sciences*, *37*(5), 455–476. https://doi.org/10.1007/s00376-020-9221-8

Gorodetskaya, I. V., Tsukernik, M., Claes, K., Ralph, M. F., Neff, W. D., & van Lipzig, N. P. M. (2014). The role of atmospheric rivers in anomalous snow accumulation in East Antarctica. *Geophysical Research Letters*, *41*, 6199–6206. https://doi.org/10.1002/2014GL060881

Guan, B., & Waliser, D. E. (2015). Detection of atmospheric rivers: Evaluation and application of an algorithm for global studies. *Journal of Geophysical Research: Atmospheres*, *120*, 12,514–12,535. https://doi.org/10.1002/2015JD024257

Guan, B., & Waliser, D. E. (2019). Tracking atmospheric rivers globally: Spatial distributions and temporal evolution of life cycle characteristics. *Journal of Geophysical Research: Atmospheres*, *124*, 12,523–12,552. https://doi.org/10.1029/2019JD031205

Guan, B., Waliser, D. E., & Ralph, F. M. (2018). An intercomparison between reanalysis and dropsonde observations of the total water vapor transport in individual atmospheric rivers. *Journal of Hydrometeorology*, *19*(2), 321–337. https://doi.org/10.1175/JHM-D-17-0114.1

Hock, T. F., & Franklin, J. L. (1999). The NCAR GPS dropwindsonde. *Bulletin of the American Meteorological Society*, *80*(3), 407–420. https://doi.org/10.1175/1520-0477(1999)080<0407:TNGD>2.0.CO;2

Hong, S. Y., & Lim, J. (2006). The WRF single-moment 6-class microphysics scheme (WSM6). *Journal of the Korean Meteorological Society*, *42*, 129–151.

Hong, S.-Y., & Pan, H.-L. (1996). Nonlocal boundary layer vertical diffusion in a medium-range forecast model. *Monthly Weather Review*, *124*(10), 2322–2339. https://doi.org/10.1175/1520-0493(1996)124,2322:NBLVDI.2.0.CO;2

Hu, H., & Dominguez, F. (2019). Understanding the role of tropical moisture in atmospheric rivers. *Journal of Geophysical Research: Atmospheres*, *124*, 13,826–13,842. https://doi.org/10.1029/2019JD030867

Hu, H., Dominguez, F., Wang, Z., Lavers, D. A., Zhang, G., & Ralph, F. M. (2017). Linking atmospheric river hydrological impacts on the U. S. West Coast to Rossby wave breaking. *Journal of Climate*, *30*(9), 3381–3399. https://doi.org/10.1175/JCLI-D-16-0386.1

Huffman, G. J., Bolvin, D. T., & Nelkin, E. J. (2018). Integrated multi-satellite retrievals for GPM (IMERG) technical documentation. Accessed 5 January 2020, https://pmm.nasa.gov/sites/default/files/document_files/IMERG_doc_180207.pdf

Insua-Costa, D., & Miguez-Macho, G. (2018). A new moisture tagging capability in the Weather Research and Forecasting model: Formulation, validation and application to the 2014 Great Lake-effect snowstorm. *Earth System Dynamics*, *9*, 167–185. https://doi.org/10.5194/esd-2017-80

Joyce, R. J., Janowiak, J. E., & Huffman, G. J. (2001). Latitudinal and seasonal dependent zenith angle corrections for geostationary satellite IR brightness temperatures. *Journal of Applied Meteorology*, *40*(4), 689–703. https://doi.org/10.1175/1520-0450(2001)040<0689:LASDZA>2.0.CO;2

Joyce, R. J., Xie, P., & Janowiak, J. E. (2011). Kalman filter based CMORPH. *Journal of Hydrometeorology*, *12*(6), 1547–1563. https://doi.org/10.1175/JHM-D-11-022.1

Kain, J. S. (2004). The Kain–Fritsch convective parameterization: An update. *Journal of Applied Meteorology*, *43*(1), 170–181. https://doi.org/10.1175/1520-0450(2004)043<0170:TKCPAU>2.0.CO;2

Knippertz, P., Wernli, H., & Gläser, G. (2013). A global climatology of tropical moisture exports. *Journal of Climate*, *26*(10), 3031–3045. https://doi.org/10.1175/JCLI-D-12-00401.1

Lavers, D. A., Allan, R. P., Wood, E. F., Villarini, G., Brayshaw, D. J., & Wade, A. J. (2011). Winter floods in Britain are connected to atmospheric rivers. *Geophysical Research Letters*, *38*, L23803. https://doi.org/10.1029/2011GL049783

Lavers, D. A., & Villarini, G. (2013). The nexus between atmospheric rivers and extreme precipitation across Europe. *Geophysical Research Letters*, *40*, 3259–3264. https://doi.org/10.1002/grl.50636

Leung, L. R., & Qian, Y. (2009). Atmospheric rivers induced heavy precipitation and flooding in the western U.S. simulated by the WRF regional climate model. *Geophysical Research Letters*, *36*, L03820. https://doi.org/10.1029/2008GL036445

Lundquist, J. D., Neiman, P. J., Martner, B., White, A. B., Gottas, D. J., & Ralph, F. M. (2008). Rain versus snow in the Sierra Nevada, California: Comparing Doppler profiling radar and surface observations of melting level. *Journal of Hydrometeorology*, *9*(2), 194–211. https://doi.org/10.1175/2007JHM853.1

Miguez-Macho, G., Stenchikov, G., & Robock, A. (2004). Spectral nudging to eliminate the effects of domain position and geometry in regional climate model simulations. *Journal of Geophysical Research*, *109*, D13104. https://doi.org/10.1029/2003JD004495

Nash, D., Waliser, D., Guan, B., Ye, H., & Ralph, F. M. (2018). The role of atmospheric rivers in extratropical and polar hydroclimate. *Journal of Geophysical Research: Atmospheres*, *123*, 6804–6821. https://doi.org/10.1029/2017JD028130

Neiman, P. J., Ralph, F. M., Wick, G. A., Kuo, Y., Wee, T., Ma, Z., et al. (2008). Diagnosis of an intense atmospheric river impacting the Pacific Northwest: Storm summary and offshore vertical structure observed with COSMIC satellite retrievals. *Monthly Weather Review*, *136*(11), 4398–4420. https://doi.org/10.1175/2008MWR2550.1

Neiman, P. J., Ralph, F. M., Wick, G. A., Lundquist, J. D., & Dettinger, M. D. (2008). Meteorological characteristics and overland precipitation impacts of atmospheric rivers affecting the West Coast of North America based on eight years of SSM/I satellite observations. *Journal of Hydrometeorology*, *9*(1), 22–47. https://doi.org/10.1175/2007JHM855.1

Nusbaumer, J., & Noone, D. (2018). Numerical evaluation of the modern and future origins of atmospheric river moisture over the West Coast of the United States. *Journal of Geophysical Research: Atmospheres*, *123*, 6423–6442. https://doi.org/10.1029/2017JD028081

Paltan, H., Waliser, D., Lim, W. H., Guan, B., Yamazaki, D., Pant, R., & Dadson, S. (2017). Global floods and water availability driven by atmospheric rivers. *Geophysical Research Letters*, *44*, 10,387–10,395. https://doi.org/10.1002/2017GL074882

Ralph, F. M., Dettinger, M. D., Cairns, M. M., Galarneau, T. J., & Eylander, J. (2018). Defining "atmospheric river": How the glossary of meteorology helped resolve a debate. *Bulletin of the American Meteorological Society*, *99*(4), 837–839. https://doi.org/10.1175/BAMS-D-17-0157.1

Ralph, F. M., Iacobellis, S. F., Neiman, P. J., Cordeira, J. M., Spackman, J. R., Waliser, D. E., et al. (2017). Dropsonde observations of total integrated water vapor transport within North Pacific atmospheric rivers. *Journal of Hydrometeorology*, *18*(9), 2577–2596. https://doi.org/10.1175/JHM-D-17-0036.1

Ralph, F. M., Neiman, P. J., Kiladis, G. N., Weickmann, K., & Reynolds, D. W. (2011). A multiscale observational case study of a Pacific atmospheric river exhibiting tropical–extratropical connections and a mesoscale frontal wave. *Monthly Weather Review*, *139*(4), 1169–1189. https://doi.org/10.1175/2010MWR3596.1

Ralph, F. M., Neiman, P. J., & Rotunno, R. (2005). Dropsonde observations in low-level jets over the northeastern Pacific Ocean from CALJET-1998 and PACJET-2001: Mean vertical-profile and atmospheric-river characteristics. *Monthly Weather Review*, *133*(4), 889–910. https://doi.org/10.1175/MWR2896.1

Ralph, F. M., Neiman, P. J., & Wick, G. A. (2004). Satellite and CALJET aircraft observations of atmospheric rivers over the eastern north Pacific Ocean during the winter of 1997/98. *Monthly Weather Review*, *132*(7), 1721–1745. https://doi.org/10.1175/1520-0493(2004)132<1721:SACAOO>2.0.CO;2

Ralph, F. M., Nieman, P. J., Wick, G. A., Gutman, S. I., Dettinger, M. D., Cayan, D. R., & White, A. B. (2006). Flooding on California's Russian River: Role of atmospheric rivers. *Geophysical Research Letters*, *33*, L13801. https://doi.org/10.1029/2006GL026689

Ralph, F. M., Rutz, J. J., Cordeira, J. M., Dettinger, M., Anderson, M., Reynolds, D., et al. (2019). A scale to characterize the strength and impacts of atmospheric rivers. *Bulletin of the American Meteorological Society*, *100*(2), 269–289. https://doi.org/10.1175/BAMS-D-18-0023.1

Ramos, A. M., Trigo, R. M., Liberato, M. L. R., & Tome, R. (2015). Daily precipitation extreme events in the Iberian Peninsula and its association with atmospheric rivers. *Journal of Hydrometeorology*, *16*(2), 579–597. https://doi.org/10.1175/JHM-D-14-0103.1

Ryoo, J.-M., Chiao, S., Spackman, J. R., Iraci, L. T., Ralph, F. M., Martin, A., et al. (2020). Terrain trapped airflows and precipitation variability during an atmospheric river event. *Journal of Hydrometeorology*, *21*(2), 355–375. https://doi.org/10.1175/JHM-D-19-0040.1

Ryoo, J.-M., Waliser, D. E., Waugh, D. W., Wong, S., Fetzer, E. J., & Fung, I. (2015). Classification of atmospheric river events on the U.S. West Coast using a trajectory model, 1–22. https://doi.org/10.1002/(ISSN)2169-8996

Shields, C. A., Rutz, J. J., Leung, L. Y., Ralph, F. M., Wehner, M., Kawzenuk, B., et al. (2018). Atmospheric River Tracking Method Intercomparison Project (ARTMIP): Project goals and experimental design. *Geoscientific Model Development*, *11*(6), 2455–2474. https://doi.org/10.5194/gmd-11-2455-2018

Sodemann, H., Masson-Delmotte, V., Schwierz, C., Vinther, B. M., & Wernli, H. (2008). Interannual variability of Greenland winter precipitation sources: 2. Effects of North Atlantic Oscillation variability on stable isotopes in precipitation. *Journal of Geophysical Research*, *113*, D12111. https://doi.org/10.1029/2007JD009416

Stohl, A., Forster, C., & Sodemann, H. (2008). Remote sources of water vapor forming precipitation on the Norwegian west coast at 60 degrees N—A tale of hurricanes and an atmospheric river. *Journal of Geophysical Research*, *113*, D05102. https://doi.org/10.1029/2007JD009006

UCAR. (2020). AVAPS Dropsonde system. https://www.eol.ucar.edu/observing_facilities/avaps-dropsonde-system

Viale, M., & Nunez, M. N. (2011). Climatology of winter orographic precipitation over the subtropical Central Andes and associated synoptic and regional characteristics. *Journal of Hydrometeorology*, *12*(4), 481–507. https://doi.org/10.1175/2010JHM1284.1

Viale, M., Valenzuela, R., Garreaud, R. D., & Ralph, F. M. (2018). Impacts of atmospheric rivers on precipitation in southern South America. *Journal of Hydrometeorology*, *19*(10), 1671–1687. https://doi.org/10.1175/JHM-D-18-0006.1

Waliser, D., & Guan, B. (2017). Extreme winds and precipitation during landfall of atmospheric rivers. *Nature Geoscience*, *10*(3), 179–183. https://doi.org/10.1038/ngeo2894

Wille, J. D., Favier, V., Dufour, A., Gorodetskaya, I. V., Turner, J., Agosta, C., & Codron, F. (2019). West Antarctic surface melt triggered by atmospheric rivers. *Nature Geoscience*, *12*(11), 911–916. https://doi.org/10.1038/s41561-019-0460-1

Zhu, Y., & Newell, R. E. (1998). A proposed algorithm for moisture fluxes from atmospheric rivers. *Monthly Weather Review*, *126*(3), 725–735. https://doi.org/10.1175/1520-0493(1998)126<0725:APAFMF>2.0.CO;2